Materials Science & Engineering A 618 (2014) 118–128

Contents lists available at ScienceDirect

Materials Science & Engineering A

journal homepage: www.elsevier.com/locate/msea

Comparison of nanoindentation techniques for local mechanical quantification of aluminium alloy

Vlastimil Králík *, Jiří Němeček

Czech Technical University in Prague, Faculty of Civil Engineering, Department of Mechanics, Thákurova 2077/7, 166 29 Prague, Czech Republic

ARTICLE INFO

Article history:
Received 30 May 2014
Received in revised form
14 August 2014
Accepted 16 August 2014
Available online 16 September 2014

Keywords:
Nanoindentation
Micromechanical properties
Elastic properties
Hardness
Modulus mapping
Aluminium foam

ABSTRACT

Nanoindentation is widely used for the assessment of micromechanical behaviour of multiple phases within the material microstructure. Structural materials typically exhibit large variations in elastic modulus and hardness with increasing indentation depth during depth-sensing indentation experiments because the measured stiffness response is affected by its heterogeneity. In this study, the complicated microstructure of heterogeneous aluminium foam cell walls is described and related micromechanical analyses using various characterization modes performed. The paper compares the results of several nanoindentation approaches for the assessment of hardness and elastic parameters using both the quasi-static indentation and the dynamic modulus mapping method. The results of quasi-static indentation were performed for two different indenter geometries (Berkovich and spherical tips). The material phase properties were analysed with grid indentation method based on statistical evaluation of a large number of indentations (statistical deconvolution technique) as well as with isolated indentations by spherical indenter that revealed overall properties of the foam cell wall. Special attention was paid to the volume affected by the indenter and other factors influencing reliable evaluation of nanoindentation measurements. Intrinsic properties of the individual phases were also verified with modulus mapping technique. Results from the dynamic measurements were consistent with the values obtained in quasi-static measurements using the Berkovich indenter for both main microstructural phases.

1. Introduction

Proper knowledge of mechanical properties of a multi-phase material is very important for an advanced material design and application. Nanoindentation has now become a standard experimental technique for evaluating the mechanical properties of the wide range of materials such as metals, glass, ceramics and thin films in small volumes (e.g. elastic moduli and hardness [1]). It also can be used to derive strain-hardening exponents, fracture toughness, and viscoelastic properties of materials [2]. Nanoindentation is based on the measurement of the load versus penetration relationship using a very small indenter tip, which is forced into the material. The main advantage in comparison with conventional mechanical testing is that material parameters are obtained from a very small volume, typically from tens of nanometres to micrometres. Different kinds of indenters can be used for making an imprint into the material surface (spherical, pyramidal, flat and others).

In general, nanoindentation provides results from a locally homogenized volume at microscale. However, its use for heterogeneous and porous materials such as metal foams or composite structural materials, which can reveal the micromechanical properties of individual phases (components), is still limited. Standard nanoindentation data processing is based on an assumption of homogeneous and isotropic half-space without a scale limit. In contrast, the properties obtained from indentation data of a heterogeneous material are averaged quantities dependent on the type of an indenter and on the indentation depth.

Structural materials show several types of heterogeneity at microscale. The heterogeneity can originate from mixing of unreacting components or from chemical reactions that are evolving after the mixing. Aluminium foam is a material with both these heterogeneities and material properties of the foam cell walls are affected by adding various stabilizing and foaming agents [3] to molten metal during the manufacturing process. The overall behaviour of aluminium foam is directly dependent on the formation of the individual phases and their micro-properties [4].

This work was initiated to investigate the applicability of the different nanoindentation techniques for measuring cell wall mechanical properties of a thin-walled cellular alloy – Alporas [3]. Although it is generally accepted that the nanoindentation test

* Corresponding author. Tel.: +420 224 35 4328; fax: +420 224 31 0775.
E-mail addresses: vlastimil.kralik@fsv.cvut.cz (V. Králík), jiri.nemecek@fsv.cvut.cz (J. Němeček).

http://dx.doi.org/10.1016/j.msea.2014.08.036
0921-5093/

can be used for measuring elastic and plastic properties of the thin cell walls [4–7], extensive experimental studies comparing different approaches and influencing factors are still lacking. In previous studies conducted by the authors it was found that the nanoindentation can describe phase elastic properties of heterogeneous cell walls using advanced evaluation methods such as statistical deconvolution [8].

In this study, the three indentation approaches for measuring the mechanical properties are shown in details with its advantages and disadvantages. Hardness and elastic modulus of the foam cell wall were measured using both the quasi-static indentation [1,2] and the modulus mapping method [9,10]. The results of quasi-static indentation were compared for two different indenter geometries. Special attention was paid to the volume affected by the indenter and other factors influencing reliable evaluation of the measurements.

2. Material

Aluminium foams are characterized by the system of opened or closed pores and very thin cell walls. The fraction of pore space in the foam may take over 90% of the sample volume [3,11,12]. Closed-cell aluminium foam (trade name Alporas produced by Shinko Wire Company Ltd., Japan) with the overall porosity of 91% was used in this study.

The manufacturing process of the Alporas is a batch casting process [3] in which 0.2–8% [11] (1.5 wt% in our sample) of calcium is added to the aluminium molten at 680 °C. Calcium serves as a thickening agent which increases viscosity and stabilizes the air bubbles. The Al alloy is poured into a casting mould and stirred with an admixture of 1–3% [11] (1.6 wt% in our sample) TiH_2 that is used as a blowing agent. Then, the foamed molten material is cooled down. Both elements Ti and Ca remain in the aluminium matrix in the form of new compounds (precipitates of mainly Al_4Ca and $TiAl_3$) after processing. A typical resulting internal structure of the aluminium foam is shown on different scales in Fig. 1a. The Alporas foam is characterized by a hierarchical microstructure. At least two characteristic length scales can be distinguished: the cell wall level (microscopic) and the foam level (macroscopic). Prediction of macroscopic properties on the whole foam level is directly dependent on the morphology of cells and the material properties of cell walls. Morphology of cell walls is quite complex and was dealt with many studies in the past [5,13–16]. Simone et al. [15] and Sugimura et al. [5] have found that many of the cell walls in aluminium foam (Alporas and Alcan foams) have some initial curvature [15] as well as small voids within them [5,15]. There are local regions of higher density where the cell walls are thicker at the nodes. The cell walls are sometimes corrugated, especially in the lower density materials [5,15,16]. The structure of the cell walls can be characterized in terms of the cell wall thickness and its position variation. It typically ranges from tens to several hundreds of microns [5,13,15] depending on the type of Al-alloy, porosity and production process. It should be pointed out that the wall thickness is usually much larger than a typical size of an indent and thus the wall geometry does not play a significant role in our investigations where we deal with microscopic (cell wall) properties measured by nanoindentation. For large indentations, the wall thickness and shape should always be confronted with the indentation size.

2.1. Microstructure characterization

The microstructure of the aluminium foam cell wall was studied in an electron scanning microscope (SEM). The non-homogeneous solid phase of the cell wall is shown in Fig. 1b. Two distinct phases, that exhibit different colour in back-scattered electron (BSE) images, can be distinguished in the Alporas foam cell walls. The phases include an aluminium alloy matrix and a precipitate phase. The chemical composition of both phases was checked with energy-dispersive X-ray elemental analysis in SEM. The matrix which occupies the majority of the volume (dark zone in Fig. 1b) consists of aluminium (~67 wt%), oxygen (~32 wt%)

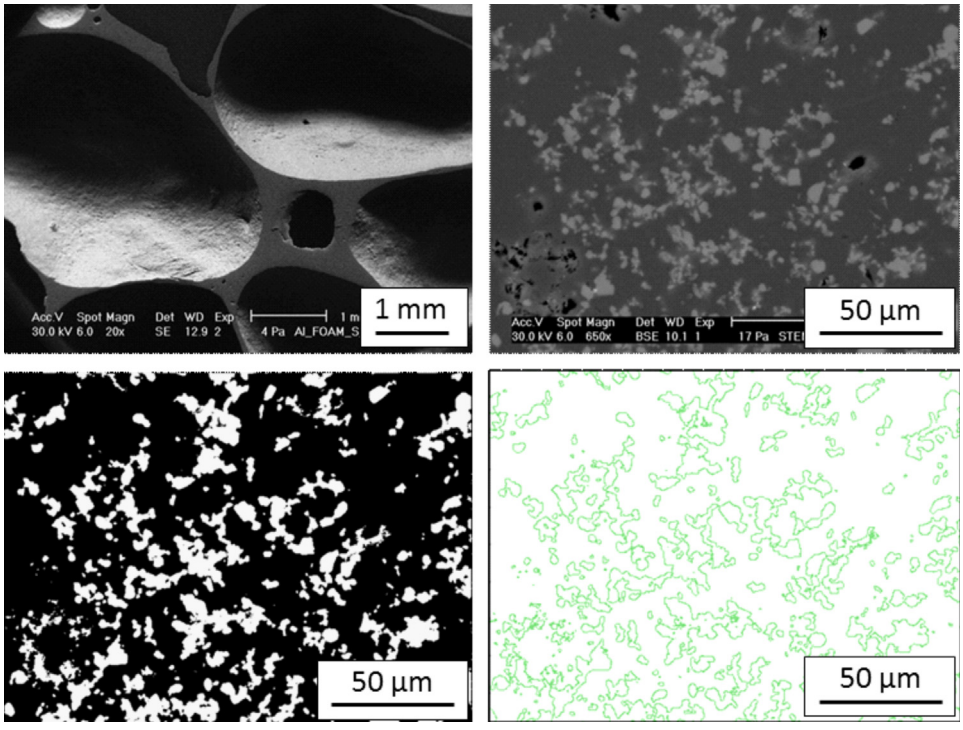

Fig. 1. (a) An example of foam cellular structure, (b) SEM image of the cell wall showing Al-rich (dark grey) and Ca/Ti-rich areas (light zones), (c) image segmented to two phases (Al-rich – black, Ca/Ti-rich – white), (d) completely recognized contours of Ca/Ti rich phases in Matlab.

and a small amount of trace elements (Mg, Ti, Fe, Co, Ni, Cu, Si <2 wt%) in solid solution. Lighter zones in Fig. 1b consist of Al ($\sim$60 wt%), O ($\sim$30 wt%), Ca ($\sim$5 wt%), Ti ($\sim$5 wt%) and other elements (<1 wt%). As expected, the majority of the volume (dark zone) is composed of aluminium and aluminium oxide Al_2O_3 (further denoted as Al-rich area). Lighter zones contain significant amount of calcium and titanium. These areas, denoted as Ca/Ti-rich, contain dendritic network of precipitates such as Al_4Ca or $TiAl_3$ [15]. The overall distribution of the precipitate phase (Ca/Ti rich) through the foam sample was quite uniform. There was no apparent difference between the precipitate density in the cell wall bulk and in the cell edge. The overall incidence of the precipitate phase shows on isotropic mixing of the admixtures that are added during the production process.

To determine the optimal parameters of the indentation it is necessary to estimate the characteristic sizes of each of these phases and their volume fractions. For this purpose, an image analysis based on SEM images of cell walls was applied. Eight images from randomly selected areas were investigated. The images were segmented to two phases using a common threshold value of a grey level for all images Fig. 1c. Using image analysis in Matlab, an equivalent diameter of inclusions assuming circular shape of Ca/Ti phases was calculated in the range of 1.4–22.6 μm and the characteristic size of inclusion was estimated as 4.46 ± 0.3 μm. This shows a significant variance in the size of inclusions, but it is generally in agreement with the literature [5]. For example, Sugimura et al. [5] provides in his study estimate of the characteristic size of the Ca/Ti phase (approximately 10 μm) and the characteristic grain size of primary Al-rich area (approximately 20 μm in diameter). The Ca/Ti-rich area was estimated to cover 19 ± 3% of the whole area. This result is in good agreement with the value (15%) reported for Alporas e.g. by Simone et al. [15].

2.2. Morphology of cell walls

Alporas is characterized with closed pore structure [12]. The cell edges and walls are curved and corrugated, indicating that the cells have solidified before equilibrium configurations could be reached. The edges have a continuously decreasing cross-sectional area from the nodal points (where they meet other edges) towards their mid-span [16], which is shown in Fig. 1a.

The most important parameter for the description of the cell wall structure is the distribution of cell wall thicknesses. This geometrical parameter is crucial for the selection of optimal parameters of the indentation. For this purpose, a high resolution optical image of the Alporas foam surface on a cross-section embedded to blackwashed gypsum was prepared. Prior to imaging the surface of specimen was grinded to remove defects which have arisen during cutting. It was mechanically polished with SiC papers to receive smooth and flat surface. The size of the scanned area was 112×158 mm^2 (which is sufficiently large to represent a structural level of the material). The cell wall thickness assessed as the minimum distance between neighbouring pores was evaluated using image analysis. Its distribution is shown in Fig. 2. It shows a significant peak, i.e. a characteristic thickness, around $\sim$61 μm, which is in agreement with the experimental value reported by Sugimura et al. [5] (85 μm for Alporas with relative density 0.08 with composition of 5 wt% of Ca and 3 wt% of TiH_2) and Simone et al. [15] (82 μm). The majority of cell wall thicknesses lies between 20 and 200 μm.

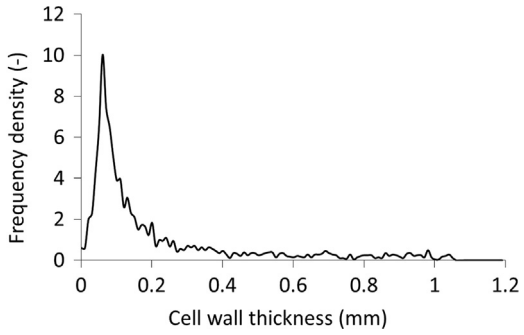

Fig. 2. Distribution of cell wall thickness.

3. Nanoindentation techniques – theory

There is a variety of indentation modes that are all resting upon exploring load-penetration diagram acquired during the test [2]. From that, variety of local material parameters like elastic (elastic modulus, hardness), plastic (strain-hardening exponents, yield strength), fracture toughness or viscous can be extracted [2]. For the convenience of the reader, we give a brief overview and the description of main technique features in this chapter.

3.1. Quasi-static indentation

Standardly, the elastic and inelastic material constants are derived from nanoindentation data using analytical solutions typically applicable to homogeneous and isotropic half-space with a flat surface. The elastic contact problem was solved already by Hertz [17] in 1882 when he found the solution of elastic contact of two spheres with different radii. In 1965 Sneddon [18] derived a general relationship between load, displacement and contact area for any punch described as a solid of revolution of a smooth function.

The theoretical solutions for elastic indentation of isotropic half-space presented here are valid for a conical indenter shape. However other similar tip shapes can be used for testing. Then, the correction shape factor has to be introduced in the mathematical relationships. The pure Sneddon's solution [18] for a cone gives:

$$P = \frac{\pi a}{2} E_r a \cot \alpha \tag{1}$$

where P is an applied load, E_r is an indentation modulus, a is contact radius and α is a cone semi-angle as shown in Fig. 3 with the surface deflection [8]:

$$h = \left(\frac{\pi}{2} - \frac{r}{a}\right) a \cot \alpha \quad for\ r \le a \tag{2}$$

Two elastic constants are usually derived from experimental data: hardness and elastic modulus. Hardness is defined as the mean contact pressure at maximum load [2]:

$$H = \frac{P_{max}}{A} \tag{3}$$

in which A is the projected contact area of the indenter at the peak.

During loading, the material under the indenter deforms both elastically and plastically. Upon unloading, however, only the elastic deformation can be assumed in most cases, which allows the calculation of an effective local stiffness of the material known as the indentation or reduced modulus, E_r. From the experiments

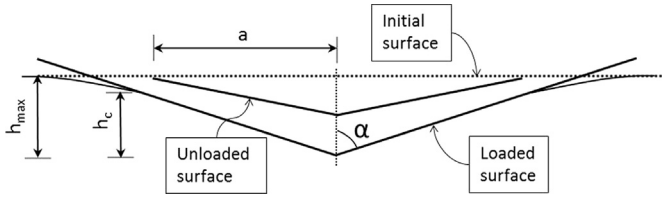

Fig. 3. Scheme of the situation under the indenter [8].

we get maximum force P_{max}, maximum deflection h_{max} and slope at the peak $dP/dh|_{P_{max}}$. The reduced modulus is then determined from an initial part of the unloading curve as [2]:

$$E_r = \frac{1}{2}\frac{\sqrt{\pi}\,dP}{\sqrt{A}\,dh} \tag{4}$$

Using contact mechanics (Hertz's solution of two non-rigid bodies), the reduced modulus can be related to the sample elastic modulus E through the following relation [2]:

$$\frac{1}{E_r} = \frac{(1-\nu^2)}{E} + \frac{(1-\nu_i^2)}{E_i} \tag{5}$$

where ν is Poisson's ratio of the tested material, E_i and ν_i are elastic modulus and Poisson's ratio of the indenter (known), respectively.

The problem with analysing experimental data is the proper fitting of the unloading branch and contact area under the indenter. Probably the most popular evaluation methodology was reported by Oliver and Pharr [1] in which the contact depth is given by:

$$h_c = h_{max} - \varepsilon\frac{P_{max}}{dP/dh} \tag{6}$$

where ε is a constant that depends on the indenter geometry (ε=0.75 for Berkovich and spherical indenter). Hardness can be computed according to Eq. (3) and the reduced modulus as [1]:

$$E_r = \frac{1}{2\beta}\frac{\sqrt{\pi}\,dP}{\sqrt{A}\,dh} \tag{7}$$

where β is a geometrical factor to correct non-symmetrical indenter shape (for Berkovich indenter β=1.034 and for spherical indenter β=1.0).

Eqs. (3), (6) and (7) are valid for elastic as well as elastic–plastic indentation and any rotationally symmetric indenter shape. For elastic contact with a spherical indenter of nominal radius R (Fig. 4) Hertz's formulae [19] may be applied, too:

$$\frac{P}{\pi a^2} = \frac{4}{3\pi}E_r\left(\frac{a}{R}\right),\ a = \sqrt{2Rh_c - h_c^2},\ h = \sqrt[3]{\frac{9P^2}{16RE_r}},\ h_c = \frac{h}{2} \tag{8}$$

3.2. Dynamic measurements

The dynamic method (nanoDMA) is based on a simple one-degree-of-freedom model of the indented sample which includes the sample stiffness K_s and the damping C_s, as well as the stiffness K_i and the damping C_i of the indentation system, Fig. 5.

In the nanoDMA, a dynamic force $P(t)=P_0 \sin \omega t$ with amplitude P_0 and frequency $f=\omega/2\pi$ is superimposed on quasi-static loading P_{max}. For a sinusoidal indentation (driving) force and

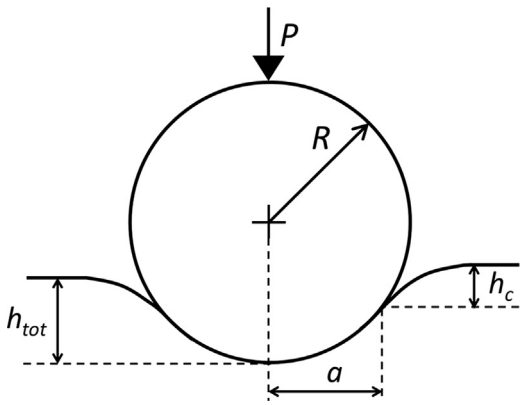

Fig. 4. Indentation by a spherical indenter [8].

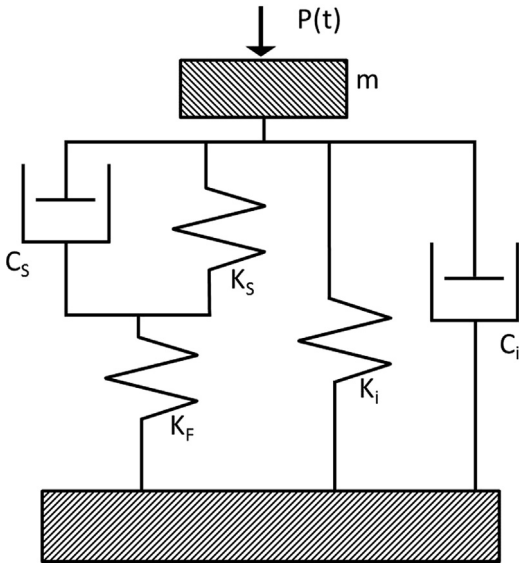

Fig. 5. Dynamic model of the indenter system in contact with specimen where m is the indenter mass, C_i is the damping coefficient of the indentation system in ambient air, C_s is the damping coefficient of the specimen, K_s is the contact stiffness, K_i is the spring constant of the leaf springs that hold the indenter and K_F is the frame stiffness ($K_F \to \infty$) [9].

alternating angular frequency ω the equation of motion of the indenter relative to the indenter head is [9]:

$$m\ddot{h} + C\dot{h} + Kh = P_0 \sin \omega t \tag{9}$$

The solution to the above equation is a steady-state displacement oscillation at the same frequency as the excitation [9]:

$$h = h_0 \sin(\omega t - \phi) \tag{10}$$

where h_0 is the amplitude of the displacement oscillation and ϕ is the phase shift of the displacement with respect to the driving force. The amplitude and phase shift can be used to calculate the contact stiffness in the indentation system (Fig. 5). The standard analytical solution for this model, assuming that the frame stiffness K_F is infinite, follows. The amplitude of the tip displacement h_0 and the phase shift ϕ are given by [9]

$$h_0 = \frac{P_0}{\sqrt{(K_S + K_i - m\omega^2)^2 + ((C_i + C_S)\omega)^2}},\ \phi = \tan^{-1}\frac{(C_i + C_S)\omega}{K_S + K_i - m\omega^2} \tag{11}$$

Values of stiffness and damping of the sample can be determined from Eq. (11). Subsequently, the viscoelastic properties, reduced storage (E_r') and loss (E_r'') moduli and their ratio $\tan\delta = E_r''/E_r'$, are computed from the relationships [9]:

$$E_r' = \frac{K_S\sqrt{\pi}}{2\sqrt{A}},\ E_r'' = \frac{\omega C_S\sqrt{\pi}}{2\sqrt{A}},\ \tan\delta = \frac{E_r''}{E_r'} = \frac{\omega C_S}{K_S} \tag{12}$$

where A is the contact area based on indenter area function related to the contact depth at quasi-static test. The storage modulus depends on the elastic recovery of the sample, which is the amount of energy recovered from the sample subsequent to a loading cycle (i.e. stiffness of the material). The loss modulus relates to the damping behaviour of the material and is demonstrated by the time lag between the maximum force and the maximum displacement. The ratio of the loss modulus to the storage modulus ($\tan\delta$) reflects the degree of viscosity of the material. It is a material parameter independent of the indenter-sample contact area.

The storage and loss moduli of the sample E_s' and E_s'' are related to the reduced characteristics by the same relationships as in

Eq. (5) for quasi-static indentation. Following the solution of Eq. (9) both storage and loss moduli give rise to overall sample characterization through complex modulus $E_s^* = E_s' + iE_s''$.

NanoDMA measurement can be performed on a larger sample area by using so called modulus mapping technique. It combines an in-situ imaging capabilities with the ability to perform dynamic tests of a nanoindenter instrument. During the imaging process, the system continuously monitors the dynamic characteristics of the sample (E_s^*, E_s', E_s'') as a function of the position. Therefore, at each image pixel (typically 256×256 px.), the storage and loss moduli are found if the geometry of the indenter is known. At the same time one can also gain information about the sample surface morphology.

4. Key parameters of individual techniques

4.1. Influence of the indenter shape

Different shapes of probes are used for nanoindentation testing. Nanoindentation hardness tests are generally made with either spherical or pyramidal indenters. The standard three-sided pyramidal indenter is the Berkovich indenter. The Berkovich indenter has a total included angle (plane to edge) of 142.3° and a half angle of 65.35° [2]. With an aspect ratio of 1:8, the Berkovich indenter is designed to have the same depth to area ratio as the Vickers indenter (microindentation standard). Because of the smaller aspect ratio and sharper indenter, the Berkovich indenter is typically used with samples where the plastic deformation must be confined to a much smaller volume such as ultra-thin films. Due to the sharp angle at the end of the indenter, the Berkovich indenter is also ideal for high resolution in-situ SPM imaging, which is essential for modulus mapping technique.

With a pyramidal indenter, the ratio of the length of contact diagonal to the depth of penetration remains constant for increasing indenter load. This principle is widely used in hardness measurements, where the value of hardness is independent of the applied load. For spherical indenters, the radius of the circle of contact increases faster than the depth of penetration as the load increases. This can be used to obtain the response of the larger area of tested material below the indenter (see Section 4.3). The same value for mean contact pressure (hardness) may be obtained with different radii of indenters and different loads as long as the ratio of the radius of the circle of contact to the nominal radius of the indenter (a/R) is the same in each case.

Stresses develop differently during indentation when using a spherical indenter compared to either a Berkovich or Vickers indenters. For spherical indenters, the contact stresses are initially small and produce only elastic deformations. As the spherical indenter is driven into the surface, a transition from elastic to plastic deformation occurs, which can theoretically be used to examine yielding and work hardening, and to recreate the entire uniaxial stress–strain curve from data obtained in a single test [8]. Nanoindentation with spherical tips has been most successfully employed with larger-diameter indenters. At the micron scale, the use of spherical indenters has been affected by insufficient quality of spheres made from rigid materials.

4.2. Influence of the exact geometry of the indenter

The correct determination of material properties by any indenter depends on the exact knowledge of its geometry. The Berkovich indenter is used routinely for nanoindentation testing because the sharp point is produced more easily than in the case of Vickers geometry. This ensures a more precise control over the indentation process. The indenter radius for a typical Berkovich ranges between 50–200 nm [2]. For quasi-static measurements, it is usually recommended to perform testing at depths that are larger than the indenter radius, i.e. in the range where the tip was calibrated for. In case of modulus mapping technique, where the depths and amplitudes of penetration are very small, one needs to estimate the Berkovich indenter radius or contact area function also for small depths. It can be obtained using similar procedures used for calibration of the spherical indenter, i.e. assuming spherical shape at the apex.

In case of a spherical indenter, the situation is more complex. The indenter shape often deviates from spherical one (ideal shape) and the radius is not constant, especially for small tip radii and small depths of penetration. This difference can be quite large as illustrated in Figs. 6 and 7.

Therefore, an accurate indenter calibration is crucial for correct determination of the material parameters by spherical indenters, especially for small depths of penetration. One of the possibilities to receive the contact area is by imaging the imprints with scanning or atomic force microscope. More often, the "indenter area function" $A(h_c)$ is calculated from the contact stiffness obtained by indenting a sample of known reduced modulus, for example using fused silica (as in our experiment) at various contact depths. The contact area for each contact depths is calculated by rearranging Eq. (7). The measured $A(h_c)$ values are then approximated by a suitable analytical expression, e.g. a polynomial [1]:

$$A(h_c) = C_0 h_c^2 + C_1 h_c + C_2 h_c^{1/2} + C_3 h_c^{1/4} + C_4 h_c^{1/8} + C_5 h_c^{1/16} \quad (13)$$

where h_c is the contact depth and C_0–C_5 are polynomial constants. In the case of a spherical indenter (assuming that its shape is close the ideal) one can use the relationship [2]:

$$A(h_c) = \pi a^2 = \pi\left(2Rh_c - h_c^2\right) \approx 2\pi R h_c \quad (14)$$

where R is the nominal indenter radius. Once we know the indenter area function $A(h_c)$, it is possible to evaluate the hardness and reduced modulus of the sample material. It should be noted that in case of an imperfect shape of a spherical indenter one can

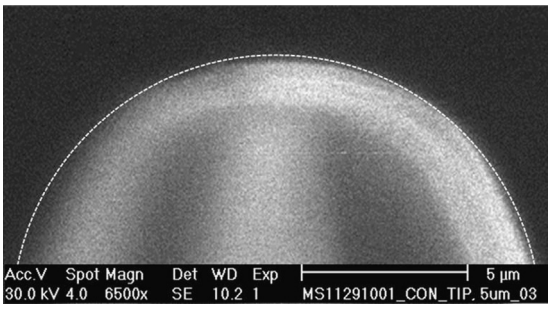

Fig. 6. SEM image of a diamond spheroconical indenter of nominal radius 5 µm (dotted line – ideal radius).

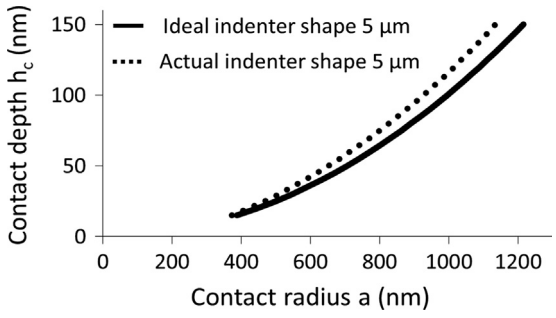

Fig. 7. Contact depth as a function of actual contact radius of a spherical indenter with 5 µm nominal radius.

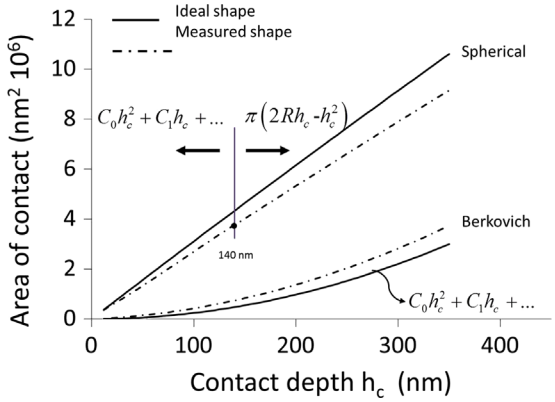

Fig. 8. Comparison of indenter area functions (spherical shape and Berkovich).

use Eq. (13) only to a maximum depth of contact for which it was calibrated. For larger depths one should apply Eq. (14).

Comparison of the indenter area functions for Berkovich and spherical tip with $R=5$ μm is shown in Fig. 8. For our case, maximum calibration depth of spherical indenter with $R=5$ μm was 140 nm. Eq. (13) was used for calibration below this value, whereas Eq. (14) was used further as shown in Fig. 8.

4.3. Choice of the penetration depth

As stated earlier, the properties obtained from indentation data of a heterogeneous material are averaged quantities dependent on the indentation depth. The size of the affected indentation volume can be estimated from the examination of elastic–plastic indentation stress fields in the interior of the specimen. The indentation stress fields arise from the pressure distributions, which are applied over a contact radius on the surface. The stress field associated with variety of indenters can be determined analytically for a linearly elastic half-space [2,8]. The affected volume under the indenter has approximately a spherical shape.

The analysis of elastic stress fields presented by [2] shows that the size of the affected volume generated by indentation of a flat surface by a spherical indenter is similar to size of the affected volume generated by pyramidal indenter for the same contact area. However, due to the geometry of a spherical indenter, the contact area is considerably larger at the same depth of penetration compared to Berkovich tip as illustrated in Fig. 8. Simultaneously, the stress-affected material volume under the spherical tip is significantly greater at the same depth of penetration than that for Berkovich indenter.

To quantify the differences in the affected volume in case of an elasto-plastic material, FE model was used. The FE simulation of the nanoindentation test (with spherical and Berkovich tips) was performed using a rotationally axisymmetric model. All parts of the model were meshed using 4-nodes plane elements with linear shape functions. A layer of contact elements was inserted between the sample and the tip. The mesh was substantially refined in the proximity of the tip contact (the size of elements under the tip was 0.074 μm whereas elements at boundary were 2 μm wide). Both indenters were modelled with known pure elastic material constants. For the specimen (Alporas) an elasto-plastic material model with isotropic linear hardening was assumed (i.e. bilinear stress–strain diagram). The considered material model is described by 4 material constants: Young's modulus ($E=75$ GPa) and Poisson's ratio ($\nu=0.2$), yield point ($\sigma_y=75$ MPa) and a hardening parameter (tangent modulus $E_{tan}=1000$ MPa) using vonMises yield criterion and isotropic linear hardening. More detailed description of the FE model can be found in [20]. Plots of an equivalent vonMises stress under the indenters are shown in Fig. 9 for a fixed maximum

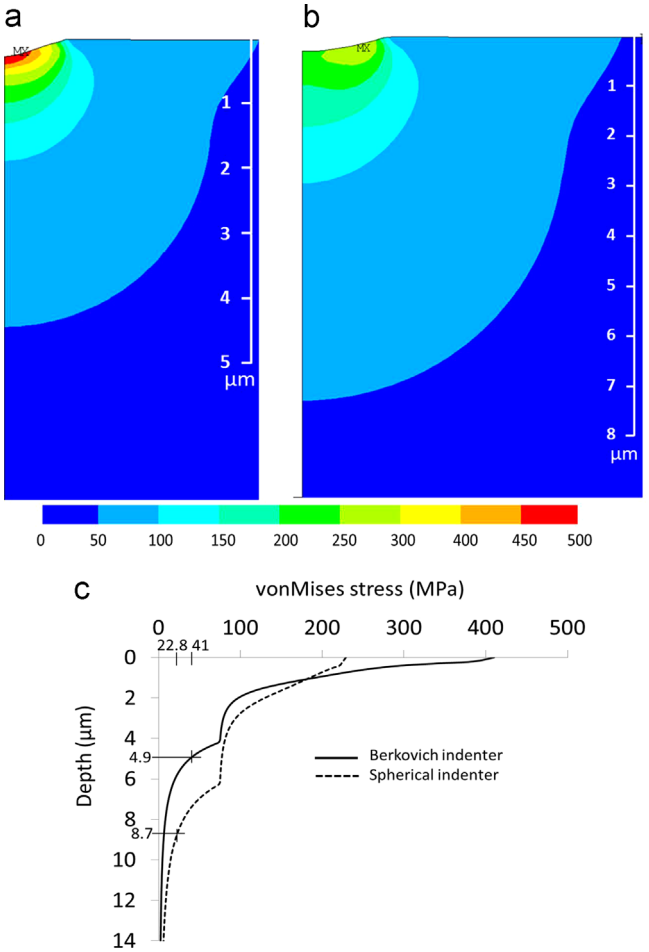

Fig. 9. Comparison of an equivalent vonMises stress for maximum indenter penetration depth 270 nm under the indenter (values in MPa). (a) Stress plot for Berkovich, (b) stress plot for sphere, (c) stress profile on the symmetry axis.

penetration depth ($h=270$ nm). It can be seen in Fig. 9a,b that the stress affected zone under the indenter is larger for spherical tip compared to Berkovich. Substantial stresses develop to about 4–7 μm under the tips. The affected depth under the spherical indenter with a nominal radius of 5 μm was found to be ~1.78 times greater than for Berkovich indenter (the ratio was computed at the 10% of the maximum stress under the tip, see Fig. 9c).

Stress curves in Fig. 9c exhibit also a characteristic turning point in their curvature at the stress level of 75 MPa. This is caused by the adoption of a simplified bilinear constitutive model that exhibits sharp transition from elastic to plastic regime.

The previous finding has important implications. In a heterogeneous material, one must carefully inspect the size of its heterogeneities with respect to the affected indentation volume. If the distinct phase properties are to be determined, Berkovich is more suitable for this task.

For largely heterogeneous materials, where the phase interactions are unavoidable or separation of phases is not clear, the statistical approach [21,22] can be successfully used to derive characteristic phase values. Massive grids in which indents are produced over a large area to capture the sample heterogeneity need to be performed. The dimension of a single indent should be much smaller than the characteristic dimension of an individual phase. For our case, the maximum depth of penetration was therefore limited to $h\sim270$ nm (using Berkovich). It yields the indent's width ~1.73 μm (obtained from indenter area function) and depth of the affected volume ~4.9 μm (obtained from FE

simulation), which roughly corresponds with the characteristic inclusion dimensions (4.46 ± 0.3 μm).

Using a spherical indenter with a nominal radius of 5 μm, the dimension of a single indent will increase considerably with the depth of penetration. In relation to the reliable indenter tip calibration, the penetration depths were chosen in the range 45–350 nm. For the maximum penetration depth ($h \sim 350$ nm), the associated individual indent's width and depth of the affected volume were ~3.4 μm (obtained from indenter area function) and ~10.03 μm (obtained from FE simulation), respectively. As shown here and mentioned above, the affected material volume under the spherical tip is considerably greater than in case of Berkovich tip. For this reason, the interaction volume exceeds the characteristic phase size and evaluated properties must be treated as average (or effective) properties for the phase compound related to this volume.

It should be also noted that the indentation depth need to be considerably smaller than the characteristic microstructural length scale (i.e. the characteristic cell wall thickness, 61 μm – see Section 2.2). As a rule of thumb the indentation depth is usually limited to 1/10 of the characteristic size [23] to comply the analytical assumptions [1]. The rule was fullfilled in our case and the affected volume (Fig. 9) under the indenter was fairly within the cell wall.

4.4. Influence of the type of loading

A typical nanoindentation loading diagram consists of loading followed by an unloading sequence. But there are many variations in the loading diagram. Load may be applied continuously until the maximum load is reached, or as a series of small increments. At each increment, a partial unloading may be programmed that provides information about the stiffness of the contact (dP/dh), which is important for measuring changes in modulus or hardness with penetration depth. Contact stiffness may also be found by superimposing a small oscillatory load onto the static one.

In the case of a spherical tip of nominal radius 5 μm where the affected area under the indenter is relatively large compared to Berkovich, the partial unloading technique was used to follow the development of elastic modulus relative to the depth. Comparison of a typical load versus indentation depth plot for a partial unloading and a single indentation is depicted in Fig. 10. Partial unloading indentation and single indentation curves fit closely which justifies evaluation of the elastic moduli from individual cycles in the partial unloading indentation diagram in this specific case.

5. Experiment

5.1. Sample preparation

Specimens for nanoindentation testing were prepared from small Alporas block $18 \times 18 \times 14$ mm^3 which was firstly embedded into cylindrical mould and filled with a low viscosity epoxy resin

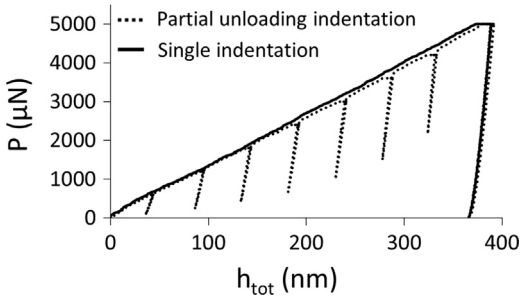

Fig. 10. Typical single and partial unloading indentation load versus depth curve (Alporas cell wall, 5 μm indenter radius).

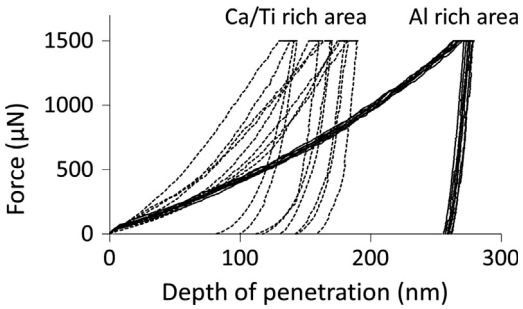

Fig. 11. Example of variation in loading diagrams for Al-rich and Ca/Ti-rich phases.

(Struers®) to fill the pores. Then, ~5 mm slice was cut by diamond saw and polished with fine SiC papers with selected technological process [24]. While preparing the specimens, special care was taken so that the opposite faces of the specimens, after final polishing, remained perfectly parallel to each other. Resulting surface roughness was checked with in-situ SPM imaging (surface scanning was performed with Berkovich tip). Quadratic deviation from the mean plane (root-mean-square [25]) was found to be $R_q \approx 9$ nm which was acceptable compared to the minimum indentation depths ~100 nm. As a rule of thumb, the surface roughness should be kept within 10% of the expected maximum depths used in quasi-static nanoindentation which was fulfilled in our case.

5.2. Experimental methods

Experiments were performed using Hysitron Tribolab system® TI 700 UbiTM located at the CTU Prague's laboratory. The nanoindenter employs a high-resolution actuator to force an indenter into the test surface and a high-resolution sensor to continuously measure the resulting penetration. The system also enables in-situ SPM imaging which was used for scanning the sample surface using a three-axis piezo positioner and nanoDMA module for dynamic testing in the range 0–300 Hz. This equipment is essential for the modulus mapping technique. The system has a load and displacement resolution of 100 nN and 0.2 nm, respectively while the maximum load and displacement are 10 mN and 5 μm, respectively. Three-sided pyramidal diamond indenter (Berkovich) was used for quasi-static measurement and modulus mapping technique while spherical indenter of nominal radius 5 μm was used for quasi-static measurement only. When using a Berkovich indenter, standard load controlled test for an individual indent consisted of three segments: loading, holding at the peak and unloading. Loading and unloading of this trapezoidal loading function lasted for 5 s, the holding part lasted for 10 s. Maximum applied load was 1500 μN. Maximum indentation depths were ranging between 75 and 296 nm depending on the stiffness of the indented phase (Fig. 11).

In the case of spherical indenter, partial unloading indentations with increasing load were performed in 8 cycles up to maximum load 5 mN. Loading time was 5 s, followed by 5 s holding period at the maximum load and unloading time 5 s, per each cycle. Single loading–unloading cycle to the maximum load was also performed for comparison.

6. Results and discussion

6.1. Quasi-static measurements with Berkovich indenter and statistical evaluation

Results from nanoindentation using Berkovich indenter clearly showed heterogeneity of the cell walls, i.e. the presence of

mechanically different inclusions (Ca/Ti precipitates). Variety of results from different positions of individual indents is shown in Fig. 11 in which a group of curves belongs to Al-rich and Ca/Ti-rich areas, respectively. The load displacement curves show some variance within the same phase. It is evident from Fig. 11 that the variation in the load displacement curves is much smaller for Al-rich phase, which occupies a larger volume in cell walls showing its relative homogeneity.

Since the mechanical properties measured on the cell wall using nanoindentation vary significantly depending on the location of penetration, producing one or more indents is not sufficient to represent the phases at the cell wall. Representative properties can be obtained by performing quite large number of indents over the cell wall and results evaluated by statistical analysis.

In total, over 200 indents performed in two distant locations were considered to give sufficiently large set of statistical data (there was no significant difference in results from both positions). Elastic moduli and hardness were evaluated for each individual indent using Eqs. (3) and (7) with standard Oliver and Pharr method [1]. Poisson's ratio needed for the estimation of elastic modulus in Eq. (6) was taken to be 0.35 for all indents (equivalent to aluminium [26]). Overall results are depicted in Fig. 12 which shows histograms of elastic moduli and hardnesses derived from all indentations. As already mentioned, large scatter in the results can be attributed to the natural heterogeneity in chemical and mechanical composition in the sample. The scatter is very large for the Ca/Ti phase and smaller for Al-rich phase. However, both histograms of elastic moduli and hardnesses clearly exhibit the bimodal character proving the existence of two mechanically distinct phases.

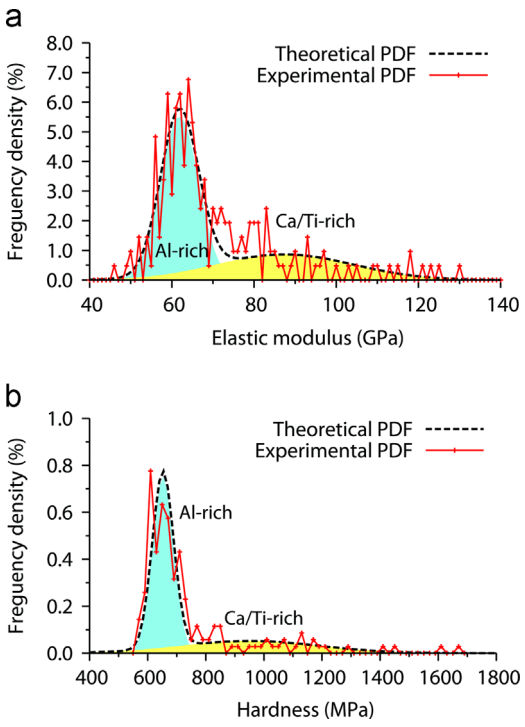

Fig. 12. Probability density functions of elastic moduli (a) and (b) hardness from merged results of two measured positions and deconvoluted phase distributions.

Individual phase properties were determined by the statistical deconvolution technique [21,23] applied to histograms of the elastic moduli and hardness values. The deconvolution procedure was adopted from [22]. The deconvolution algorithm seeks for parameters of individual phases included in overall results in the form of experimental probability density function. It searches for n-Gauss distributions and minimizing criteria of the differences between the experimental and theoretical overall probability density function of the analysed quantity to find the best fit. An assumption of the two-phase system was used in our deconvolution. Table 1 contains numerical results from the deconvolution also with the estimated volume fractions of the phases.

The characteristic value of elastic modulus for Al-rich phase can be compared to the elastic modulus of pure aluminium (70 GPa, [26]). The lower value of the elastic modulus can be affected by impurities (Ca) added to the molten material or other microstructural modifications originating from the foaming process. Although the value of elastic modulus of Al-rich phase was derived from statistical deconvolution it is in excellent agreement with the value (61.7 GPa) measured by Jeon et al. [6] on bulk samples from Al–1.5 wt% Ca alloy.

Results from statistical deconvolution were further used for calculating the effective elastic properties of the Alporas cell wall material by selected analytical homogenization schemes, namely Voigt and Reuss bounds, Mori–Tanaka method and self-consistent schemes [23,27]. The homogenized elastic modulus for the cell wall is summarized in Table 2. The estimates given by different schemes show insignificant differences.

6.2. Results of spherical nanoindentation

Fig. 13 shows representative experimental load–indentation curves for Alporas cell wall using spherical indenter of nominal radius 5 μm. A total of 35 indentations were made using a spherical tip. It is evident from Fig. 13 that the curves exhibit small dispersion, which is significantly smaller than that obtained with Berkovich indenter. This reveals the uniformity of the microstructure of Alporas cell wall on the larger scale tested with a spherical indenter. It should be noted that this uniformity is not a material property (as explained in the previous section) but it is given by the larger characteristic dimension of the indent.

Elastic moduli were evaluated for each from individual cycles in the partial unloading indentation diagram of individual indents using Eqs. (3) and (7) with standard Oliver and Pharr method [1]. Table 3 contains overall results in which the average value and

Table 2
Effective values of elastic modulus computed by different homogenization schemes.

Scheme	Mori–Tanaka	Self-consist. scheme	Voigt bound	Reuss bound
E_{eff} [GPa]	70.083	70.135	71.118	69.195

Table 1
Elastic moduli, hardness and volume fractions from deconvolution.

	Elastic modulus			Hardness		
Phase	Mean (GPa)	St. dev. (GPa)	Volume fraction	Mean (MPa)	St. dev. (MPa)	Volume fraction
1 (Al-rich zone)	61.9	4.6	0.638	654	38	0.713
2 (Ca/Ti-rich zone)	87.4	16.7	0.362	969	237	0.287

standard deviation of all elastic moduli and each cycle from different positions are shown.

For small measured contact depths (up to about 45 nm), there are considerable differences in the values of elastic moduli, indicated by a higher standard deviation. These differences may be partially caused by an imperfect indenter shape for very small contact depths and/or by surface roughness of the sample. Therefore, the results for $h_c < 45$ nm were not considered further.

The results in Table 3 indicate that the elastic modulus increases with increasing depth of penetration and affected volume under the indenter, respectively. The values of elastic modulus converge to an average value 70.0 ± 3.1 GPa which is consistent with the value obtained by analytical homogenization from statistical results of Berkovich indentation (~70.1 GPa, Table 2). The agreement gives the experimental proof of the correctness of the used analytical and numerical approaches in Section 6.1.

6.3. Results of modulus mapping

The modulus mapping measurement was accomplished by applying a small oscillation to the force signal at a relatively high frequency (170 Hz). The amplitude of the force oscillation was 9 μN and the nominal contact force was 11 μN. The corresponding displacement oscillation was monitored at the excitation frequency and the stiffness of contact was calculated from the amplitude of the displacement signal. Nominal contact force, displacement amplitude, phase shift, and topography are signals recorded at each of the 256×256 pixels of the image. A large area of 20×20 μm^2 was chosen after setting an appropriate gain for the lock-in amplifier and an initial dynamic force for the tip oscillation, along with a scan rate of 0.25 Hz. The scan size was then narrowed down to capture details of both phases and their interfaces and a smaller scan was performed as shown in Fig. 14. The Ti-precipitate could be identified at the left side in the figure. The figure shows the surface topography, amplitude of the tip displacement, phase shift of the displacement with respect to the driving force and gradient of the tip displacement. The surface topography is reconstructed directly from the tip displacement sensor and registers the surface roughness and grain boundaries. The displacement amplitude and phase shift is acquired as a result of force modulation and serves for the assessment of stiffness and damping characteristics of a sample using Eq. (11). From this information, the values of storage and loss moduli (see Section 3.2) are calculated for each image pixel from Eqs. (12) and (5). The gradient of the tip displacement is computed to demonstrate the rate of the quantity change between the neighbouring pixels. Quantitative variations in the aforementioned values are shown as different colours in Fig. 14.

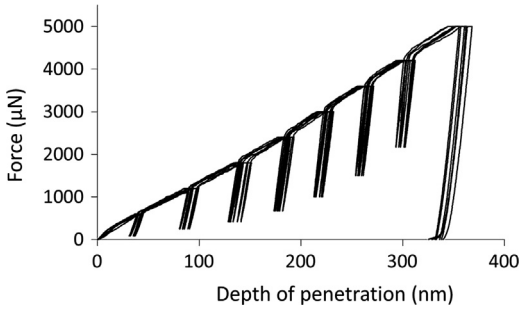

Fig. 13. Typical partial unloading diagrams (Alporas cell wall, 5 μm indenter radius).

Table 3
Spherical indenter – elastic moduli per each cycle.

No. of cycle	Average contact depth (nm)	Mean E (GPa)	St. dev. (GPa)
1	45	57.7	6.2
2	91	61.2	3.7
3	136	62.5	2.9
4	177	63.5	2.7
5	215	64.2	2.7
6	252	64.2	3.0
7	288	64.0	3.8
8	336	70.0	3.1

Due to small sample viscosity, the loss components (loss moduli) were relatively small compared to storage components, suggesting that the storage modulus is practically equal to the elastic modulus evaluated in the quasi-static case. The map of storage moduli in the selected area is depicted in Fig. 15. In this image, quantitative variations in storage moduli within the area are shown by different colours. It is easy to observe that the higher storage modulus of the Ti-precipitate significantly decreases when entering the Al-rich area around the grain. However, notable local variations in both phases could be observed from the map as illustrated also in the profile drawn across the both phases (Fig. 15). It is obvious from images of topography and gradient of the tip displacement (see Fig. 14) that the transition between the two phases is not straight and there are some areas of poor surface quality. Therefore image contains also some artifacts which occur in particular in these locations. These out-of-scale values (modulus greater than ~120 GPa) that occur on the boundaries between the phases were not considered in the evaluation. Storage moduli appearing in a particle/matrix transition were computed in a selected band (Fig. 15a) and are presented in a profile in Fig. 15b.

Average storage moduli of individual phases were derived from their respective frequency histograms as shown in Fig. 16 and fitted with normal distributions. The average magnitudes of storage moduli for Al-rich phase and Ti-rich precipitate were

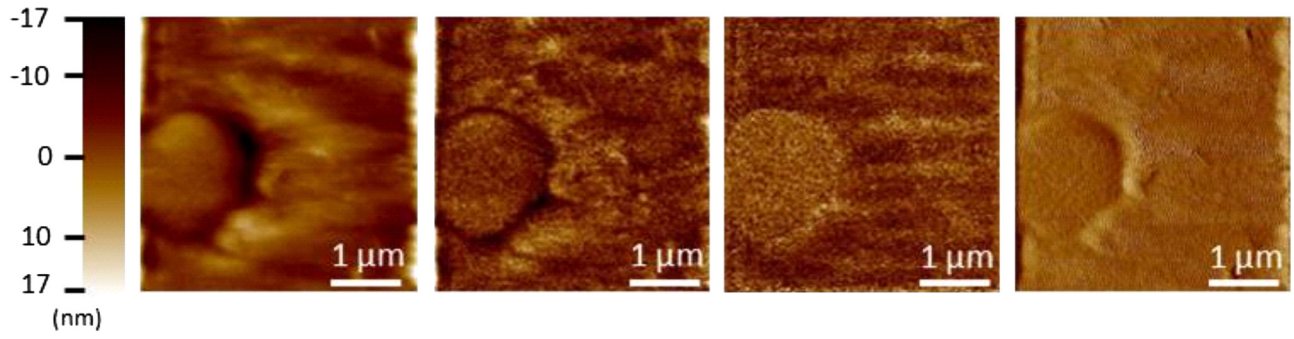

Fig. 14. Scan images obtained by in-situ imaging (left to right: topography; amplitude of the tip displacement; phase shift of the displacement with respect to the driving force; gradient of the tip displacement). (For interpretation of the references to colour in this figure, the reader is referred to the web version of this article.)

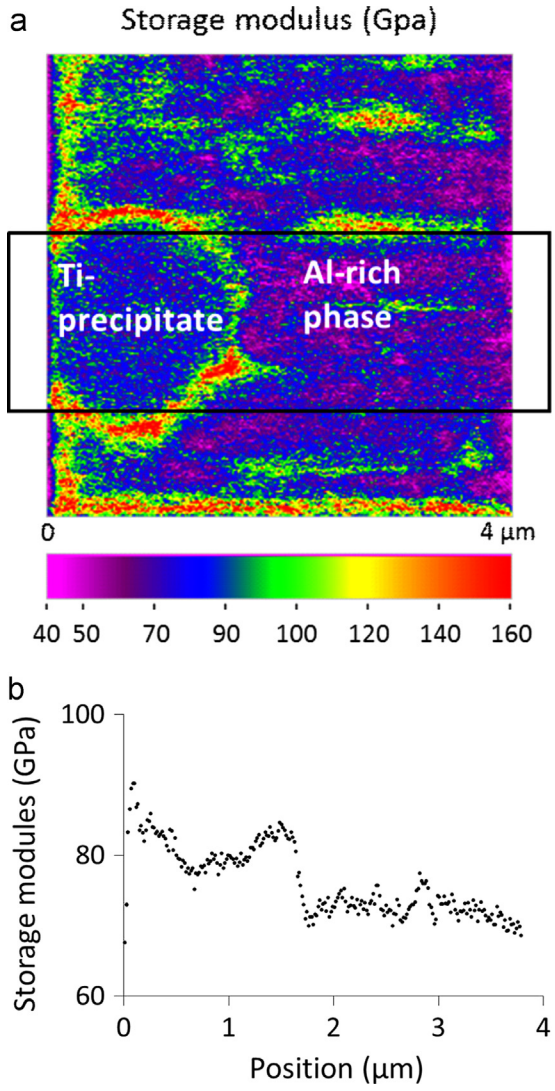

Fig. 15. (a) Storage modulus map (in GPa) and (b) its average profile in the selected band. (For interpretation of the references to colour in this figure, the reader is referred to the web version of this article.)

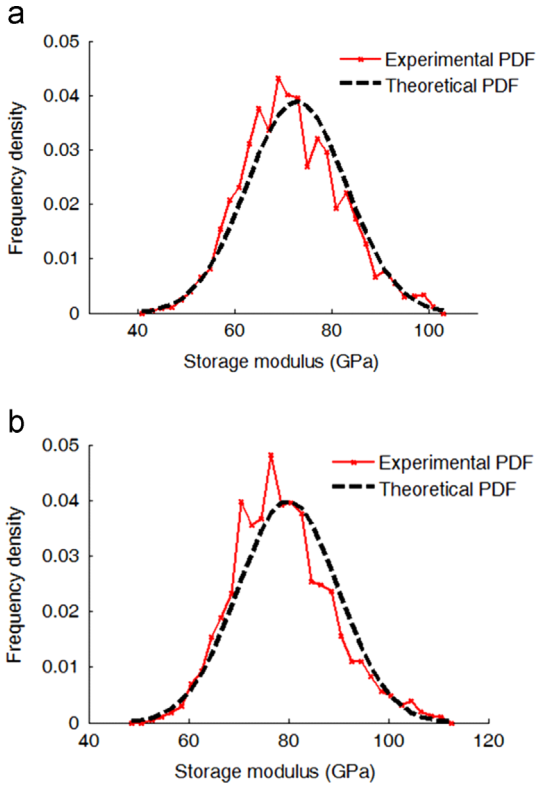

Fig. 16. Storage modulus frequency histogram for: (a) Al-rich phase; (b) Ti-precipitate.

72.8 ± 10.3 GPa and 80 ± 10 GPa, respectively. The values of storage moduli for the differently stiff regions agree well with the results obtained from statistical deconvolution results based on quasi-static measurements shown in previous sections. However, the scanned region does not represent the whole cell wall and much larger area should be covered in order to receive statistically representative values for all phases. Due to its resolution, the modulus mapping technique can be considered as the most differentiable compared to standard quasi-static tests presented earlier. On the other hand, its quantitativeness is mostly affected by the surface quality and test parameter setting.

7. Conclusions

By means of mutual comparisons, the presented investigation quantified the accuracy of three different nanoindentation techniques used to access mechanical properties of aluminium foam cell wall. The microstructure and complicated morphology of the heterogeneous material was presented and related with mechanical testing. SEM analysis revealed the presence and chemical composition of two distinct phases in aluminium cell wall (aluminium alloy matrix, the Al-rich zone, and a precipitate phase, the Ca/Ti-rich zone). An equivalent diameter of inclusions (Ca/Ti-rich zone) assuming circular shape was found to be in the range of 1.4–22.6 μm with characteristic size 4.46 ± 0.3 μm. The distribution of cell wall thicknesses was also evaluated using image analysis and the characteristic size of wall ~61 μm assessed. The results were in good agreement with the values reported by other researchers.

Key parameters of indentation technique such as the influence of loading type, influence of the exact indenter geometry, choice of the penetration depth and influence of the indenter shape were described thoroughly in this study. The analysis of elastic–plastic indentation stress fields under the indenter showed that the size of the affected volume generated by indentation of a flat surface with a spherical indenter is ~1.78 times greater than that of Berkovich for the same penetration depth. The correct determination of material properties by a spherical indenter depends also on the exact knowledge of its geometry. The indenter shape often deviates from ideal one and the radius is not constant, especially for small tip radii and small depths of penetration.

For the heterogeneous material, each indentation technique is able to evaluate the mechanical properties at different scale and different approach for the evaluation of the data is required. It was shown in the paper that results from quasi-static measurements using Berkovich indenter and small indents can disclose the presence of mechanically different inclusions. Two-phase system (major Al-rich and minor Ca/Ti-rich phase) was assumed in the statistical deconvolution algorithm to obtain elastic moduli and volume fractions of the two phases ($E_{\text{Al-rich}} = 61.9 \pm 4.6$ GPa, $E_{\text{Ca/Ti-rich}} = 87.4 \pm 16.7$ GPa). Effective elastic modulus of the whole composite was then evaluated by analytical homogenization ($E_{\text{Cell-wall}} = 70.1$ GPa).

In contrast to Berkovich indenter, the size of the affected material volume under the spherical tip with the nominal radius of 5 μm is large enough for deducing effective cell wall properties. The development of elastic modulus relative to the depth of

penetration was investigated using the partial unloading technique. The elastic modulus increases with increasing depth of penetration and affected volume under the indenter, respectively. The values of elastic moduli converge to the effective value of the wall ($E_{\text{Cell-wall}} = 70 \pm 3.1$ GPa) which is in accordance with the values acquired by homogenization from Berkovich statistical results.

Intrinsic properties of the individual phases were also obtained using dynamic measurement (modulus mapping technique) as mean values of the respective frequency histograms for Al-rich and Ti-precipitate phase ($E_{\text{Al-rich}} = 72.8 \pm 10.3$ GPa, $E_{\text{Ti-grain}} = 80 \pm 10$ GPa). These results, representing the mechanical characterization of the phases with the highest resolution, were consistent with the values obtained from quasi-static measurements using the Berkovich indenter although much larger area would have to be scanned to obtain similar statistics.

It was proven in the paper that if proper arrangements of the nanoindentation experiments in terms of proper calibration, indenter type, imprint size and loading parameters are used consistent results are obtained from a wide variety of methods. Therefore, nanoindentation can be considered as a valuable tool for accessing various material parameters on different length scales even for highly heterogeneous composition of Alporas cell walls.

Acknowledgements

Support of the Czech Science Foundation (GAČR P105/12/0824) and the Grant Agency of the Czech Technical University in Prague (SGS14/121/OHK1/2T/11) is gratefully acknowledged.

References

[1] W. Oliver, G. Pharr, J. Mater. Res. 7 (1992) 1564–1583.
[2] A.C. Fischer-Cripps, Nanoindentation, Springer, New York, 2002.
[3] T. Miyoshi, M. Itoh, S. Akiyama, A. Kitahara Aluminum Foam, "ALPORAS": The Production Process, Properties and Applications. Porous and Cellular Materials for Structure Applications, 1998, 521, pp. 133–137.
[4] M.A. Hasan, A. Kim, H.- Lee, Compos. Struct. 83 (2008) 180–188.
[5] Y. Sugimura, J. Meyer, M.Y. He, H. Bart-Smith, J. Grenstedt, A.G. Evans, Acta Mater. 45 (1997) 5245–5259.
[6] I. Jeon, K. Katou, T. Sonoda, T. Asahina, K. Kang, Mech. Mater. 41 (2009) 60–73.
[7] A. Kim, K. Tunvir, J. Mech. Sci. Technol. 20 (2006) 819–827.
[8] A.C. Fischer-Cripps, Introduction to Contact Mechanics, Springer, US, 2007.
[9] S. Asif, K. Wahl, R. Colton, Rev. Sci. Instrum. 70 (1999) 2408–2413.
[10] A. Chakravartula, K. Komvopoulos, Appl. Phys. Lett. 88 (2006) 131901.
[11] E. Andrews, W. Sanders, L.J. Gibson, Mater. Sci. Eng. A 270 (1999) 113–124.
[12] L.J. Gibson, M.F. Ashby, Cellular Solids – Structure and Properties, second edition, Cambridge University Press, Cambridge, 1997.
[13] A. Markaki, T. Clyne, Acta Mater. 49 (2001) 1677–1686.
[14] U. Ramamurty, A. Paul, Acta Mater. 52 (2004) 869–876.
[15] A.E. Simone, L.J. Gibson, Acta Mater. 46 (1998) 3109–3123.
[16] O. Prakash, H. Sang, J. Embury, Mater. Sci. Eng. A-Struct. Mater. Prop. Microstruct. Process. 199 (1995) 195–203.
[17] H. Hertz, J. Reine Angew. Math. 92 (1882) 156–171 (For English translation see Miscellaneous Papers by H. Hertz, Jones and Schott (Eds.), Macmillan, London, 1896).
[18] I.N. Sneddon, Int. J. Eng. Sci. 3 (1965) 47–57.
[19] K.L. Johnson Contact Mechanics, 1985.
[20] J. Nemecek, P. Zlamal, V. Kralik, J. Nemeckova, Civil-Comp Proc. 102 (2013), paper 103, 1–20.
[21] G. Constantinides, K.S. Ravi Chandran, F.-J. Ulm, K.J. Van Vliet, Mater. Sci. Eng. A 430 (2006) 189–202.
[22] J. Nemecek, V. Kralik, J. Vondrejc, Cem. Concr. Compos. 36 (2013) 85–92.
[23] J. Nemecek, V. Kralik, J. Vondrejc, Comput. Struct. 128 (2013) 136–145.
[24] M. Dudikova, D. Kytyr, T. Doktor, O. Jirousek, Chem. Listy 105 (2011) S790–S791.
[25] ISO 4287-1997, "Geometrical Product Specifications (GPS) – Surface Texture: Profile Method – Terms, Definitions and Surface Texture Parameters".
[26] M. Winter, WebElements: The Periodic Table on the Web, 2012. Available from: ⟨http://www.webelements.com⟩.
[27] A. Zaoui, J. Eng. Mech.-ASCE 128 (2002) 808–816.